WAVELET BEM ON MOLECULAR SURFACES — PARAMETRIZATION AND IMPLEMENTATION

HELMUT HARBRECHT AND MAHARAVO RANDRIANARIVONY

Abstract. The present paper is dedicated to the rapid solution of boundary integral equations arising from solvation continuum models. We apply a fully discrete wavelet Galerkin scheme for the computation of the apparent surface charge on van der Waals or solvent accessible surfaces. The molecular surface is described in parametric form as a set of four-sided spherical patches. Each patch is exactly represented as rational Bézier surface. Numerical results are reported to illustrate the approach.

1. Introduction

Continuum solvation models are widely used to model quantum effects of molecules in liquid solutions. In the present paper we focus on the *polarization continuum model* (PCM), introduced in [21]. In this model, the molecule under study (the solute) is located inside a cavity Ω surrounded by a homogeneous dielectric (the solvent). The solute-solvent interactions between the charge distributions which compose the solute and the dielectric are reduced to those of electrostatic origin.

The interface between the solute and the solvent constitutes the molecule's *surface*. In general, the *molecule* Ω is defined as a union of balls, centered in the nuclei positions and of radii related to the van der Waals radius. The resulting surface is called the *van der Waals surface* (VWS). Whereas, the *solvent accessible surface* (SAS) coincides with the VWS surface except for scaling of the radii. We emphasize that we do not consider *solvent excluding surfaces* (SES), also known as Connolly surfaces which are defined from the VWS model by rolling a spherical probe over the surface. Nevertheless, SES surfaces can be approximated by VWS/SAS surfaces by introducing additional spheres, see [30].

According to classical electrostatics, the charge distribution ρ of the solute, inside the molecule, polarizes the dielectric continuum, which in turn polarizes the solute's charge distribution. This interaction might be expressed in terms of an *apparent surface charge* (ASC) which resides on the molecule's surface. This is known as

Key words and phrases. Quantum chemistry, molecular surface, geometric modeling, wavelets, boundary element methods.

the ASC approach. The underlying electrostatic problem is described by a transmission problem for the Laplacian in the whole space $\mathbb{R}^3$. Therefore, the integral equation formalism (IEF) offers an advantageous approach to compute the electrostatic solute-solvent interaction. In Section 2 we briefly repeat the modelling and derive two different boundary integral equations for the apparent surface charge.

Boundary integral equations are solved in general by the boundary element method (BEM). BEM is a well established tool in PCM [3, 10, 30]. However, traditional discretizations lead to densely populated and possibly ill-conditioned system matrices. Both features pose serious obstructions to the efficient numerical treatment of such problems. Modern methods for the rapid BEM solution reduce the complexity to almost or even optimal rates. Prominent examples for such methods are the *fast multipole method* [11], the *panel clustering* [13], *$\mathcal{H}$-matrices* [12], or the *wavelet Galerkin scheme* [1, 5, 16, 28]. In fact, a Galerkin discretization with wavelet bases results in quasi-sparse matrices, i.e., most matrix entries are negligible and can be treated as zero. Discarding these nonrelevant matrix entries is called matrix compression. As shown in [5, 28] the number of significant matrix coefficients scales linearly.

The construction of wavelets on surfaces is based on a parametric representation of the surface by four-sided patches [14, 15, 16]. This surface representation is in contrast to the usual approximation of the surface by panels. It has the advantage that the geometry is exactly described. In the present paper an algorithm is developed which decomposes the molecule's surface into four-sided patches. We generate the parametrizations of the spherical patches by using rational Bézier surfaces and homogeneous coordinates. Continuity at the patch interfaces is achieved without using approximations.

We mention that there are already a lot of papers on the meshing of molecular surfaces (e.g. [20, 22, 27]). Meshing algorithms and software are meanwhile well established [4, 30]. However, these algorithms generate traditional surface approximations by planar panels and cannot be used in the present context of hierarchical bases like wavelet bases.

This paper is structured as follows. In Section 2 we derive the underlying boundary integral equations and discretize them by a wavelet based boundary element method. Section 3 is dedicated to the boundary representation (B-rep) of the molecular surface as a set of trimmed surfaces. The decomposition of the surface into smooth four-sided patches is constructed in Section 4. Finally, in Section 5, we report on numerical results which demonstrate the feasibility of the present approach.

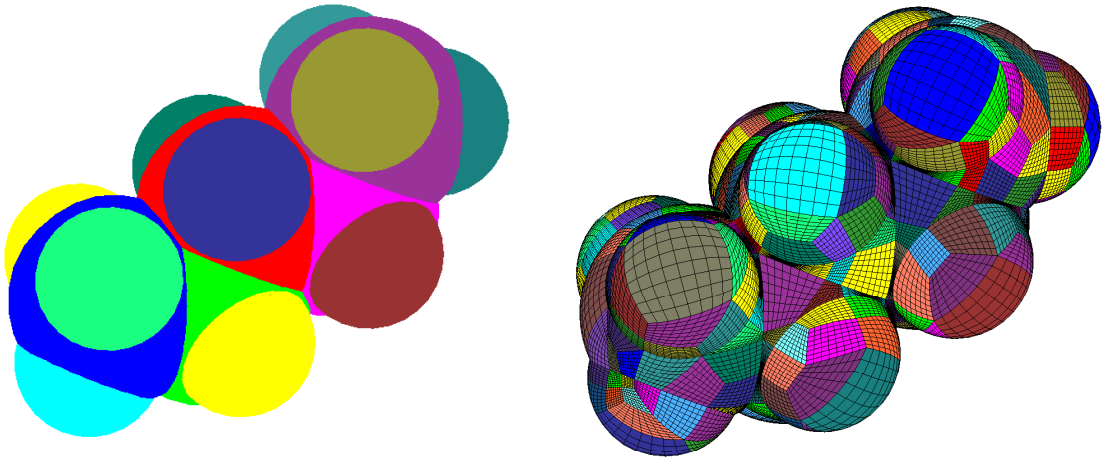

(a) (b)

FIGURE 2.1. (a) Spherical surfaces (b) Decomposition into four-sided surfaces.

2. Problem formulation

2.1. **Boundary integral equations.** We consider a cavity Ω with boundary $\Gamma = \partial\Omega$, representing the solute-solvent interface which is in our case the molecular surface. The solvent is represented by a constant dielectric medium while the solute is located inside the cavity Ω. The surface Γ of the cavity is given as van der Waals surface (VWS) model which means that each constituting atom of the molecule is represented as an imaginary sphere. The radius of each sphere corresponds to the van der Waals radius of the atom [32] or a multiple of it. We denote by $B(\mathbf{m}, r)$ the closed ball of center $\mathbf{m}$ and radius r $B(\mathbf{m}, r) := \{\mathbf{x} \in \mathbb{R}^3 : \|\mathbf{m} - \mathbf{x}\| \leq r\}$ ($\|\cdot\|$ denotes the Euclidean norm). Then, the molecule is the union of N balls

$$\Omega = \bigcup_{k=1}^{N} B(\mathbf{m}_k, r_k)$$

with $\mathbf{m}_k$ being the nuclei position and r_k being the related Van der Waal radius. The molecule's surface

$$\Gamma := \partial\Omega = \partial\left[\bigcup_{k=1}^{N} B(\mathbf{m}_k, r_k)\right], \tag{2.1}$$

is supposed to represent a single closed surface. An particular example, namely pentane, is shown in Figure 2.1.

For a given charge $\rho \in H^{-1}(\Omega)$, located inside the cavity Ω, we need to solve the following transmission problem:

$$\begin{aligned} -\Delta u_i &= \rho && \text{in } \Omega, \\ \Delta u_e &= 0 && \text{in } \Omega^c, \\ u_i = u_e,\ \frac{\partial u_i}{\partial \mathbf{n}} &= \varepsilon \frac{\partial u_e}{\partial \mathbf{n}} && \text{on } \Gamma, \\ |u_e(\mathbf{x})| &= \mathcal{O}\big(\|\mathbf{x}\|^{-1}\big) \text{ as } \|\mathbf{x}\| \to \infty. \end{aligned} \tag{2.2}$$

Herein, $\mathbf{n}$ is the outward unit normal at Γ and $\varepsilon > 0$ the macroscopic dielectric constant of the solvent outside Ω.

To solve this transmission problem by boundary integral equations we introduce the single layer operator $\mathcal{V} : H^{-1/2}(\Gamma) \to H^{1/2}(\Gamma)$ and the double layer operator $\mathcal{K} : H^{1/2}(\Gamma) \to H^{-1/2}(\Gamma)$ which are respectively defined by

$$(\mathcal{V}u)(\mathbf{x}) = \int_\Gamma \frac{u(\mathbf{y})}{4\pi\|\mathbf{x}-\mathbf{y}\|} do_{\mathbf{y}}, \quad (\mathcal{K}u)(\mathbf{x}) = \int_\Gamma \frac{\langle \mathbf{n}(\mathbf{y}), \mathbf{x}-\mathbf{y}\rangle}{4\pi\|\mathbf{x}-\mathbf{y}\|^3} u(\mathbf{y}) do_{\mathbf{y}}, \quad \mathbf{x} \in \Gamma.$$

Let further N_ρ denote the following Newton potential, defined in the whole space,

$$N_\rho(\mathbf{x}) = \int_\Omega \frac{\rho(\mathbf{y})}{4\pi\|\mathbf{x}-\mathbf{y}\|} d\mathbf{y}, \quad \mathbf{x} \in \mathbb{R}^3. \tag{2.3}$$

With these definitions at hand we find the following relations between the Dirichlet and Neumann data, called interior and exterior Dirichlet-to-Neumann maps,

$$\mathcal{V}\frac{\partial u_i}{\partial \mathbf{n}} = \Big(\frac{1}{2} + \mathcal{K}\Big) u_i - N_\rho, \quad \mathcal{V}\frac{\partial u_e}{\partial \mathbf{n}} = \Big(\mathcal{K} - \frac{1}{2}\Big) u_e, \quad \text{on } \Gamma. \tag{2.4}$$

Subtracting ε times the second boundary integral equation from the first one and inserting the Neumann jump condition (2.2), we find the following equation for the Dirichlet data u_i

$$u_i = \frac{1}{\varepsilon - 1} \mathcal{A}^{-1} N_\rho, \quad \text{where} \quad \mathcal{A} = \frac{\varepsilon + 1}{2(\varepsilon - 1)} - \mathcal{K}. \tag{2.5}$$

The physical relevant quantity is the apparent surface charge, defined by

$$\sigma = \frac{\partial u_i}{\partial \mathbf{n}} - \frac{\partial u_e}{\partial \mathbf{n}} = \frac{1-\varepsilon}{\varepsilon} \frac{\partial u_i}{\partial \mathbf{n}}. \tag{2.6}$$

To compute an related integral equation, we subtract the integral equations in (2.4) and insert the Dirichlet jump condition (2.2). This yields

$$\mathcal{V}\sigma = \Big(\frac{1}{2} + \mathcal{K}\Big) u_i - N_\rho - \Big(\mathcal{K} - \frac{1}{2}\Big) u_e = u_i - N_\rho \quad \text{on } \Gamma,$$

and thus, by (2.5), an integral equation, where only the Dirichlet data of N_ρ appear on the right hand side, namely

$$\mathcal{V}\sigma = \frac{1}{\varepsilon - 1}\mathcal{A}^{-1}N_\rho - N_\rho \quad \text{on } \Gamma. \tag{2.7}$$

To find an integral equation, where only the Neumann data of N_ρ enter the right hand side, we need to exploit the fact that the Newton potential is harmonic in Ω^c. Hence, from the exterior Dirichlet-to-Neumann map, we deduce the following relation between its Neumann and Dirichlet-data

$$\mathcal{V}\frac{\partial N_\rho}{\partial \mathbf{n}} = \Big(\mathcal{K} - \frac{1}{2}\Big)N_\rho \quad \text{on } \Gamma.$$

Inserting this relation into (2.7) and multiplying by $\mathcal{A}$ gives $\mathcal{A}\mathcal{V}\sigma = \mathcal{V}\partial N_\rho/\partial\mathbf{n}$ on Γ. By making finally use of the property $\mathcal{K}\mathcal{V} = \mathcal{V}\mathcal{K}^\star$ (see e.g. [29]) we arrive at

$$\mathcal{A}\sigma = \frac{\partial N_\rho}{\partial \mathbf{n}} \quad \text{on } \Gamma. \tag{2.8}$$

2.2. **Parametrization.** The boundary integral equations (2.7) and (2.8) are in general numerically solved by the boundary element method (BEM). Nevertheless, traditional discretizations will lead to very large linear systems with densely populated and in case of (2.7) ill-conditioned matrices. This makes the computation very costly in both respects, the computing time and memory requirements. We like to employ a discretization by wavelets which leads to quasi-sparse matrices [5, 28].

To this end, we assume that the molecular surface Γ is given as a parametric surface consisting of smooth patches. More precisely, let $\square := [0,1]^2$ denote the unit square. The surface $\Gamma \subset \mathbb{R}^3$ is partitioned into a finite number of four-sided *patches*

$$\Gamma = \bigcup_{i=1}^{M} \Gamma_i, \qquad \Gamma_i = \gamma_i(\square), \qquad i = 1, 2, \ldots, M, \tag{2.9}$$

where each $\gamma_i : \square \to \Gamma_i$ defines a diffeomorphism of $\square$ onto Γ_i. The intersection $\Gamma_i \cap \Gamma_{i'}$, $i \neq i'$, of the patches Γ_i and $\Gamma_{i'}$ is supposed to be either $\emptyset$, or a common edge or vertex.

A mesh of level j on Γ is induced by dyadic subdivisions of depth j of the unit square into 4^j squares. This generates $4^j M$ *elements* (or elementary domains) $\Gamma_{j,k}$. In order to ensure that the collection of elements $\{\Gamma_{j,k}\}_{k\in\Delta_j}$ (Δ_j denotes a suitable index set) on the level j forms a regular mesh on Γ, the parametric representation is subjected to the following *matching condition*: A bijective, affine mapping $\Xi : \square \to \square$ exists such that for all $\mathbf{x} = \gamma_i(\mathbf{s})$ on a common edge of Γ_i and $\Gamma_{i'}$ it holds that

$$\gamma_i(\mathbf{s}) = (\gamma_{i'} \circ \Xi)(\mathbf{s}). \tag{2.10}$$

In other words, the diffeomorphisms γ_i and $\gamma_{i'}$ coincide at common edges except for orientation. We emphasize that the above definitions require patchwise smoothness but *not* global smoothness of the geometry. The surface itself needs to be only Lipschitz. A graphical illustration of the surface decomposition can be found in Fig. 1(b) where we can clearly observe that two adjacent patches fulfill the above matching condition (2.10) at the interface.

2.3. **Wavelet BEM.** The nested trial spaces

$$V_0 \subset V_1 \subset \cdots \subset V_j \subset V_{j+1} \subset \cdots \subset L^2(\Gamma)$$

that we shall employ in the Galerkin scheme are the spaces of piecewise constant functions on the given partition. The trial spaces are spanned by standard piecewise constant ansatz functions $\Phi_J = \{\phi_{J,k} = \chi_{\Gamma_{J,k}} : k \in \Delta_J\}$, satisfying $N_J := |\Delta_J| \sim 4^j$. Instead of the single-scale bases Φ_J we use piecewise constant wavelets $\Psi_J = \{\psi_{j,k} : k \in \nabla_j, j < J\}$ ($\nabla_j = \Delta_{j+1} \setminus \Delta_j$) with three vanishing moments as constructed in [15].

The boundary integral equations (2.7) and (2.8) are then discretized as follows. We make the ansatz

$$\sigma \approx \boldsymbol{\sigma}_J \Psi_J = \sum_{j<J} \sum_{k \in \nabla_j} \sigma_{j,k} \psi_{j,k}$$

and introduce the system matrices

$$\mathbf{V}_J = \langle \mathcal{V} \Psi_J, \Psi_J \rangle, \qquad \mathbf{A}_J = \langle \mathcal{A} \Psi_J, \Psi_J \rangle$$

and the data vectors

$$\mathbf{f}_J = \langle N_\rho, \Psi_J \rangle, \qquad \mathbf{g} = \left\langle \frac{\partial N_\rho}{\partial \mathbf{n}}, \Psi_J \right\rangle.$$

Then, the discretized version of the boundary integral equation (2.7) corresponds to the linear system of equations

$$\mathbf{V}_J \boldsymbol{\sigma}_J = \frac{1}{1-\varepsilon} \mathbf{A}_J^{-1} \mathbf{f}_J - \mathbf{f}_J,$$

while (2.8) corresponds to

$$\mathbf{A}_J \boldsymbol{\sigma}_J = \mathbf{g}_J.$$

The system matrices in wavelet coordinates are quasi–sparse, having only $\mathcal{O}(N_J)$ relevant matrix coefficients. Applying the matrix compression strategy developed in [5, 28] combined with an exponentially convergent *hp*–quadrature method [16], the wavelet Galerkin scheme produces the approximate solutions of (2.7) and (2.8) within linear complexity. Especially, due to the norm equivalences of wavelet bases, the diagonally scaled system matrices are well posed [6, 28].

3. B-rep of Van der Waals surfaces

3.1. **Bounding circular edges.** First of all, we shall determine the boundary representation (B-rep) of the molecule's surface (2.1). To this end, it is required to find explicitly the set of edges, vertices and faces whose parametrization serves as lifting from planar decompositions.

In order to find the edges which are circular arcs, the intersections of the spheres $\mathcal{B}_k := \partial B(\mathbf{m}_k, r_k)$ need to be determined. If two spheres are not disjoint, their intersection is a circle. Thus, the first step in the generation of the B-rep structure is the computation of the circles of intersections $\mathcal{C}_i$ of non-disjoint spheres as seen in Fig. 2(b). Consider two interlocking spheres $\mathcal{B}_1 = \partial B(\mathbf{m}_1, r_1)$ and $\mathcal{B}_2 = \partial B(\mathbf{m}_2, r_2)$, where we suppose that $r_1 \geq r_2$, and let $d := \|\mathbf{m}_1 - \mathbf{m}_2\| < r_1 + r_2$ be the distance between the centers. The circle of intersection is uniquely determined by its center

$$\mathbf{M} := \mathbf{m}_1 + D\mathbf{n}, \qquad D = \frac{d^2 - r_1^2 + r_2^2}{2d},$$

its radius $R = \sqrt{r_1^2 - D^2}$ and the normal vector $\mathbf{n} = (\mathbf{m}_2 - \mathbf{m}_1)/\|\mathbf{m}_2 - \mathbf{m}_1\|$ of the plane containing the circle. In case of the molecule in Fig. 2(a) these circles of intersections are shown in Fig. 2(b).

After finding all the circles $\mathcal{C}_i$, we determine the circular arcs which represent the edges of the B-Rep structure and which are part of the circles $\mathcal{C}_i$. To find those circular arcs, we compute intersections of the circles. Note that two intersecting nonidentical circles residing on the same sphere have two points of intersections.

The set of those points of intersections which constitutes the vertices of the B-rep structure splits the circles $\mathcal{C}_i$ into a set of circular arcs $\{\mathcal{A}_i\}$. As a next step in the assembly of the B-Rep structure, we have to remove all circular arcs $\mathcal{A}_i$ which reside inside certain spheres. This can be detected by taking the midpoint $\mathbf{M}_i$ of $\mathcal{A}_i$ and testing whether $\mathbf{M}_i$ is inside some ball $B(\mathbf{m}_k, r_k)$. When all useless arcs are removed, the remaining arcs describe the edges of the B-rep of the molecular surface as illustrated in Fig. 2(c).

3.2. **On homogeneous coordinates.** We shall fix some useful notation. An element of the projective space $\mathbb{E}^3$ will be denoted as a column vector with four coordinates or as row vector whose elements are separated by colons. A point with homogeneous coordinates $[\omega : x : y : z]$ has the Cartesian coordinates $(x/\omega, y/\omega, z/\omega)$. Notice that the homogeneous coordinates

$$[\omega : x : y : z] \quad \text{and} \quad [\lambda\omega : \lambda x : \lambda y : \lambda z]$$

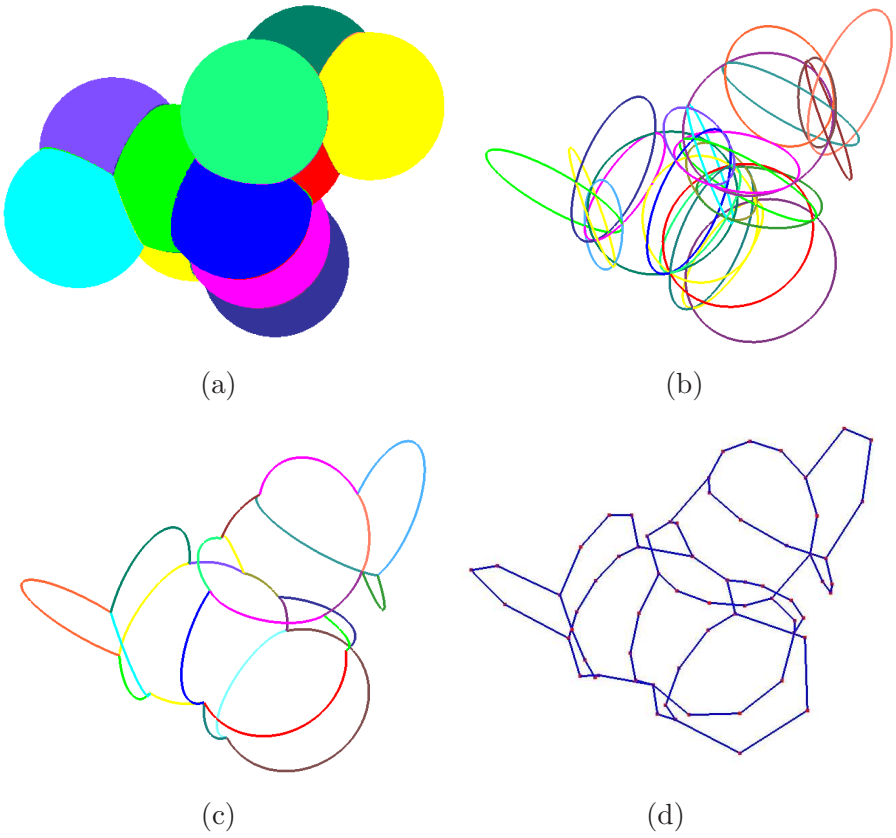

FIGURE 3.2. (a) Set of spheres (b) Circles of intersections (c) Circular arcs as edges of the B-Rep model (d) Polygonal approximation.

represent for any $\lambda \neq 0$ the same point in Cartesian coordinates. The above definitions and properties are illustrated in Fig. 3(a).

The use of homogeneous coordinates considerably simplifies theoretical formulations because rational quantities become polynomial ones which make problems linear instead of nonlinear. For example, let us consider a rational Bézier curve with weights ω_i and control points $\mathbf{b}_i = (x_i, y_i, z_i)$ in Cartesian coordinates:

$$\mathbf{X}(t) := \frac{\sum_{i=0}^{n} \omega_i \mathbf{b}_i B_i^n(t)}{\sum_{i=0}^{n} \omega_i B_i^n(t)}. \tag{3.11}$$

It corresponds to a Bézier curve having the homogeneous coordinates $[\omega_i : \omega_i x_i : \omega_i y_i : \omega_i z_i]$ in the projective space. Thus, in homogeneous coordinates the above Bézier curve is represented as

$$\mathbf{X}(t) = \sum_{i=0}^{n} [\omega_i : \omega_i x_i : \omega_i y_i : \omega_i z_i] B_i^n(t)$$

which is a linear combination of the Bernstein basis functions $B_i^n(t)$.

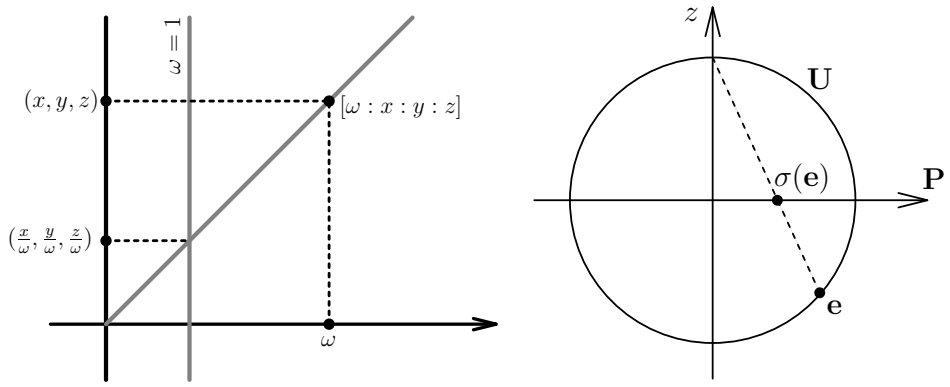

(a) (b)

FIGURE 3.3. (a) The homogeneous coordinates $[\omega : x : y : z]$ represent the Cartesian point $(x/\omega, y/\omega, z/\omega)$ (b) Stereographic projection σ from $\mathbb{S}^2$ to $\mathbb{P}$.

Vice versa, the homogeneous Bézier curve $\mathbf{X}(t) = \sum_{i=0}^{n} [\alpha_i : \beta_i : \gamma_i : \delta_i] B_i^n(t)$ corresponds uniquely (except for scaling of enumerator and denominator) to a rational Bézier curve (3.11) with $\omega_i := \alpha_i$ and $\mathbf{b}_i := (\beta_i/\alpha_i, \gamma_i/\alpha_i, \delta_i/\alpha_i)$.

Likewise, a bivariate rational Bézier $\mathbf{X}(\cdot, \cdot)$ which has the control points $\mathbf{b}_{ij} = (x_{ij}, y_{ij}, z_{ij})$ and the weights ω_{ij} (for $i = 0, 1, \ldots, n$ and $j = 0, 1, \ldots, m$) can be represented in homogeneous coordinates as

$$\mathbf{X}(u, v) = \sum_{i=0}^{n} \sum_{j=0}^{m} [\omega_{ij} : \omega_{ij} x_{ij} : \omega_{ij} y_{ij} : \omega_{ij} z_{ij}] B_i^n(u) B_j^m(v).$$

3.3. **Stereographic projection.** We shall next be concerned with the stereographic projection σ which is illustrated in Fig. 3(b). To this end, we introduce the plane $z = 0$

$$\mathbb{P} := \{[\omega : x : y : 0] \in \mathbb{E}^3 : \omega \neq 0\} = \{(x, y, z) \in \mathbb{R}^3 : z = 0\} \tag{3.12}$$

and the unit sphere

$$\mathbb{S}^2 := \{[\omega : x : y : z] \in \mathbb{E}^3 : \omega \neq 0,\ x^2 + y^2 + z^2 = \omega^2\} = \{\mathbf{x} \in \mathbb{R}^3 : \|\mathbf{x}\| = 1\}.$$

Then, the stereographic projection $\sigma : \mathbb{S}^2 \to \mathbb{P}$ maps, in Cartesian coordinates, $(x, y, z) \in \mathbb{S}^2$ to

$$\sigma(x, y, z) = \left(\frac{x}{1 - z}, \frac{y}{1 - z}, 0 \right) \in \mathbb{P},$$

see [23]. Expressed in homogeneous coordinates, $\mathbf{e} = [e_0 : e_1 : e_2 : e_3] \in \mathbb{S}^2$ is mapped to

$$\sigma(\mathbf{e}) = [e_0 - e_3 : e_1 : e_2 : 0] \in \mathbb{P}.$$

The inverse $\tau := \sigma^{-1} : \mathbb{P} \to \mathbb{S}^2$ is given by

$$\tau(x,y,z) = \left(\frac{2x}{x^2+y^2+1}, \frac{2y}{x^2+y^2+1}, \frac{x^2+y^2-1}{x^2+y^2+1} \right) \in \mathbb{S}^2$$

which is in homogeneous coordinates equivalent to

$$\tau(\mathbf{e}) = \left[e_0^2 + e_1^2 + e_2^2 : 2e_0e_1 : 2e_0e_2 : e_1^2 + e_2^2 - e_0^2 \right] \in \mathbb{S}^2.$$

Suppose that the Bézier curve $\mathbf{X} \subset \mathbb{S}^2$ is given in homogeneous coordinates by

$$\mathbf{X}(t) = \sum_{i=0}^{n} [\omega_i : \omega_i x_i : \omega_i y_i : \omega_i z_i] B_i^n(t)$$

with $z_i \neq 1$ for all i. Then, the stereographic projection maps $\mathbf{X}(t)$ onto

$$\mathbf{Y}(t) = \sigma\big(\mathbf{X}(t)\big) = \begin{bmatrix} \sum_{i=0}^n (\omega_i - \omega_i z_i) B_i^n(t) \\ \sum_{i=0}^n \omega_i x_i B_i^n(t) \\ \sum_{i=0}^n \omega_i y_i B_i^n(t) \\ 0 \end{bmatrix} = \begin{bmatrix} \sum_{i=0}^n \widetilde{\omega}_i B_i^n(t) \\ \sum_{i=0}^n \widetilde{\omega}_i \widetilde{x}_i B_i^n(t) \\ \sum_{i=0}^n \widetilde{\omega}_i \widetilde{y}_i B_i^n(t) \\ 0 \end{bmatrix} \in \mathbb{P}$$

where $\widetilde{\omega}_i := \omega_i(1-z_i)$ and $\widetilde{\mathbf{b}}_i := (\widetilde{x}_i, \widetilde{y}_i, 0) := \big(x_i/(1-z_i), y_i/(1-z_i), 0\big)$. In other words, the preimage with respect to τ of the curve of $\mathbf{X} \subset \mathbb{S}^2$ is the rational Bézier curve

$$\mathbf{Y}(t) = \frac{\sum_{i=0}^n \widetilde{\omega}_i \widetilde{\mathbf{b}}_i B_i^n(t)}{\sum_{i=0}^n \widetilde{\omega}_i B_i^n(t)} \in \mathbb{P}. \tag{3.13}$$

3.4. **Parametrizing the trimmed surfaces.** In order to complete the B-rep structure and to use it in the surface decomposition, we need to find its faces together with their parametrizations. Incident circular arcs split the sphere $\mathcal{B}_k$ into p_k subsurfaces $\mathcal{D}_i^{(k)} \subset \mathcal{B}_k$ where $i = 1, \ldots, p_k$. By removing all subsurfaces which are contained inside other spheres, the set $\{\mathcal{D}_k\}$ of the remaining subsurfaces forms the spherical faces of the B-Rep structure

$$\Gamma = \bigcup_{k=1}^{N} \mathcal{D}_k. \tag{3.14}$$

Each subsurface $\mathcal{D}_k$ (which is not necessarily four-sided) is bounded by some circular arcs $\mathcal{A}_i$. That is, there exists an index set $\mathcal{I}_k$ such that

$$\partial \mathcal{D}_k = \bigcup_{j \in \mathcal{I}_k} \mathcal{A}_j \quad \text{for all} \quad k = 1, \ldots, N.$$

We shall exploit the stereographic projection σ to represent a surface $\mathcal{D}_k$ as a parametric trimmed surface defined on some planar domain. To this end, let us denote by σ_k the analogue of the stereographic projection σ with respect to an arbitrary sphere $\mathcal{B}_k = \partial B(\mathbf{m}_k, r_k)$. According to Subsection 3.3, setting $\tau_k := \sigma_k^{-1}$, we can

compute the curves $\mathcal{E}_j = \tau_k(\mathcal{A}_j) \subset \mathbb{P}$ for each circular arc $\mathcal{A}_j \subset \mathcal{B}_k$ with $j \in \mathcal{I}_k$. Denoting by $\mathcal{F}_k$ the planar trimmed domain bounded by $\partial\mathcal{F}_k = \bigcup_{j\in\mathcal{I}_k} \mathcal{E}_j$ we thus have constructed the trimmed surface [2, 17]

$$\tau_k : \mathcal{F}_k \to \mathcal{B}_k \quad \text{with} \quad \mathcal{D}_k = \tau_k(\mathcal{F}_k) \quad \text{for all} \quad k = 1, \ldots, N. \tag{3.15}$$

Note that the preimage by τ_k of a 3D circular arc is a 2D circular arc as illustrated in Fig. 4(a) and Fig. 4(b).

4. Decomposition into four-sided spherical patches

4.1. **Polyhedral model.** To solve the integral equations (2.7) and (2.8) by the wavelet Galerkin method, we need to tessellate the molecular surface Γ into M four-sided patches according to (2.9). In order to keep the computational cost low, we claim for keeping the number M of patches is small. Basically, based on the B-rep (3.15), we perform the four-sided splitting in the planar domain $\mathcal{F}_k$ and lift the result to the molecular surface by the parametrization τ_k.

To derive this decomposition, we approximate first the curved boundaries of $\{\mathcal{D}_k\}_{k=1}^N$ by straight line segments separated by nodes $\{\mathbf{x}_i\} \subset \mathbb{R}^3$ as seen in Fig. 2(d). To ensure a conforming splitting, we create planar polygonalizations of $\{\mathcal{F}_k\}_{k=1}^N$ which amounts to the following. For each trimmed surface $\mathcal{D}_k$, we generate a polygon $\mathcal{Q}_k \subset \mathbb{P}$ whose nodes $\mathbf{x}_i^{(k)}$ are taken from the curved boundary of the planar domain $\mathcal{F}_k$. We have to make sure that for two adjacent surfaces $\mathcal{D}_k$ and $\mathcal{D}_\ell$ sharing a 3D circular arc $\mathcal{C}$, if $\tau_k(\mathbf{x}_i^{(k)}) \in \mathcal{C}$, there must exist a vertex $\mathbf{x}_j^{(\ell)} \in \mathbb{P}_\ell$ such that

$$\tau_k(\mathbf{x}_i^{(k)}) = \tau_\ell(\mathbf{x}_j^{(\ell)}). \tag{4.16}$$

Let us mention that if we take too few vertices $\mathbf{x}_i^{(k)}$, the resulting polygon $\mathcal{Q}_k$ might have imperfections such that its edges do not form an admissible polygon, as illustrated in Fig. 4(c). On the other hand, if the polygonal approximation is too fine, then it results in too many four-sided patches. As a consequence, one has to split the curved edges adaptively while maintaining the relation (4.16). We emphasize that only polygons having an *even* number of boundary vertices can be decomposed into quadrilaterals. It is not straightforward to convert odd faces into even ones inside a closed surface with arbitrary genus. We assemble the adjacency graph which is used in the Dijkstra algorithm (see, e.g., [19]) to search for the shortest path joining two odd polygons in order not to insert too many additional nodes. For closed surfaces it is proven that the number of odd faces is even and that the odd faces can be converted pairwise to even ones. We refer the reader to [24, 25] for further details.

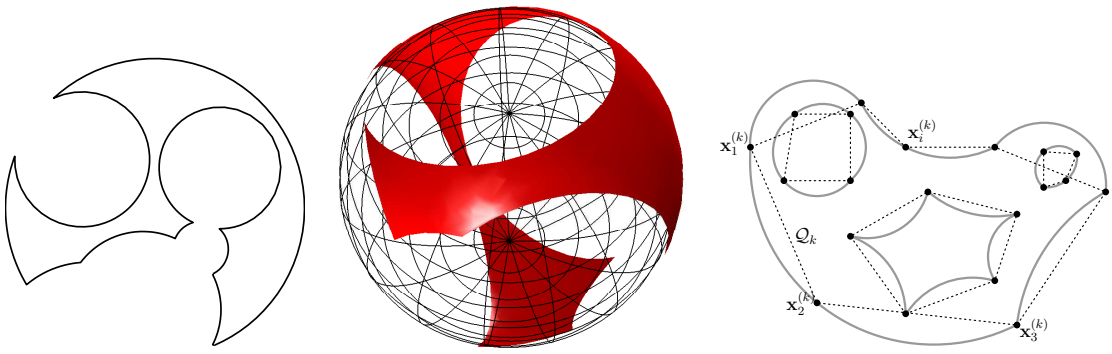

(a) (b) (c)

FIGURE 4.4. (a) Multiply connected domain with composite circular arc as boundary (b) Spherical trimmed surface (c) Imperfections in polygonal approximation.

4.2. **Quadrangulation and decomposition.** We consider a polygon $\mathcal{Q}_k \subset \mathbb{P}$ with nodes $\{\mathbf{q}_i^{(k)}\}$ which should be decomposed into a set of convex quadrilaterals $\{\mathcal{S}_i^{(k)}\}$. We use only the points $\mathbf{q}_i^{(k)}$ as boundary vertices of the $\{\mathcal{S}_i^{(k)}\}$. That is, we do only introduce nodes in the interior of $\mathcal{Q}$ during the quadrangulation process. We have developed in [24] an algorithm that decomposes a polygon with n boundary vertices into $\mathcal{O}(n)$ convex quadrilaterals.

Consider a convex quadrilateral $\mathcal{S} = [\mathbf{s}_1, \mathbf{s}_2, \mathbf{s}_3, \mathbf{s}_4]$ which is a member of the quadrangulation of the polygon $\mathcal{Q}_k$. We want now to describe how to find the corresponding four-sided patch $\mathcal{T}$ on the sphere $\mathcal{B}_k$. The four vertices of the spherical patch $\mathcal{T}$ are given by $\tau_k(\mathbf{s}_1)$, $\tau_k(\mathbf{s}_2)$, $\tau_k(\mathbf{s}_3)$, $\tau_k(\mathbf{s}_4)$. The four circular edges $\mathcal{E}_1, \mathcal{E}_2, \mathcal{E}_3, \mathcal{E}_4$ of $\mathcal{T}$ are defined as follows. If both $\mathbf{s}_i$ and $\mathbf{s}_{i+1}$ are located on $\partial\mathcal{F}_k$, then the edge $\mathcal{E}_i$ joining $\tau_k(\mathbf{s}_i)$ and $\tau_k(\mathbf{s}_{i+1})$ will be the 3D circular arc corresponding to the 2D circular arc of $\partial\mathcal{F}_k$. Otherwise, we choose the edge $\mathcal{E}_i$ as the circular geodesic that connects $\tau_k(\mathbf{s}_i)$ and $\tau_k(\mathbf{s}_{i+1})$.

4.3. **Projection on the unit sphere $\mathbb{S}^2$.** We are now going to parametrize the spherical patches as rational Bézier polynomials for the following reasons. All spherical patches with circular edges can be exactly represented as rational Bézier polynomial (cf. Fig. 5(a)). Moreover, global continuity at the patch interfaces can be accomplished (cf. Fig. 5(b)). According to our experience, spherical patches with geodesic boundary curves have very good visual properties. But the present method applies to any circular boundary, that is, each edge is the intersection of a sphere and a plane. Although we restrict ourselves to the unit sphere $\mathbb{S}^2$, they can easily be generalized to any non-degenerated sphere with minor modifications.

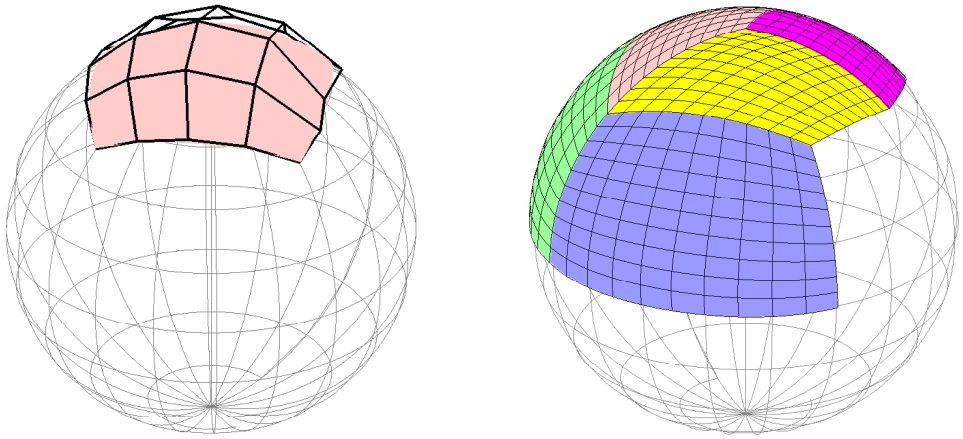

(a) (b)

FIGURE 4.5. (a) A spherical patch as rational Bézier and its control net (b) Globally continuous spherical rational Bézier patches.

The generation of the spherical mappings makes use of the next projections [8]. First, the hyperbolic projection $\vartheta : \mathbb{E}^3 \to \mathbb{P}$ maps the point $\mathbf{e} = [e_0 : e_1 : e_2 : e_3] \in \mathbb{E}^3$ to the point

$$\vartheta(\mathbf{e}) := \left[e_0^2 + e_3^2 : e_0e_1 - e_2e_3 : e_1e_3 + e_0e_2 : 0\right] \in \mathbb{P}.$$

The inverse $\delta : \mathbb{E}^3 \to \mathbb{S}^2$ of the *generalized* stereographic projection is given by

$$\delta(\mathbf{e}) := \left[e_0^2 + e_1^2 + e_2^2 + e_3^2 : 2e_0e_1 - 2e_2e_3 : 2e_1e_3 + 2e_0e_2 : e_1^2 + e_2^2 - e_0^2 - e_3^2\right].$$

The following composition and image properties hold:

$$\mathbb{P} = \vartheta(\mathbb{E}^3), \qquad \mathbb{S}^2 = \delta(\mathbb{E}^3), \qquad \sigma \circ \delta = \vartheta. \tag{4.17}$$

For two points $\mathbf{p} = [p_0 : p_1 : p_2 : p_3]$ and $\mathbf{q} = [q_0 : q_1 : q_2 : q_3]$, we define the inner product $\langle \mathbf{p}, \mathbf{q} \rangle := \sum_{i=0}^{3} p_i q_i$. Moreover, for any given $\mathbf{q} = [q_0 : q_1 : q_2 : q_3]$, let us introduce

$$\overline{\mathbf{q}} := [q_2 : q_3 : -q_0 : -q_1], \qquad \mathbf{q}^{\perp} := [-q_3 : q_2 : -q_1 : q_0].$$

Then, one readily verifies that

$$\langle \mathbf{q}, \overline{\mathbf{q}} \rangle = \langle \mathbf{q}, \mathbf{q}^{\perp} \rangle = \langle \mathbf{q}, \overline{\mathbf{q}}^{\perp} \rangle = 0. \tag{4.18}$$

The set of preimages of a point $\mathbf{p} \in \mathbb{S}^2$ is the following projective line

$$\delta^{-1}(\mathbf{p}) = \{\lambda \mathbf{q} + \mu \mathbf{q}^{\perp} : \lambda, \mu \in \mathbb{R}\}, \tag{4.19}$$

where $\mathbf{q} \in \mathbb{R}^3$ is any preimage of $\mathbf{p}$. Especially the point

$$\mathbf{p} = [1 : \sin\theta\cos\varphi : \sin\theta\sin\varphi : \cos\theta] \in \mathbb{S}^2$$

owns the particular preimage $\mathbf{q} \in \mathbb{E}^3$ given by

$$\begin{aligned} q_0 &= \sin^2\theta \\ q_1 &= (1+\cos\theta)(\sin\theta\cos\varphi + \cos\theta\sin\varphi) \\ q_2 &= (1+\cos\theta)(\sin\theta\sin\varphi - \cos\theta\cos\varphi) \\ q_3 &= \sin\theta\cos\theta. \end{aligned} \tag{4.20}$$

Notice that, due to the mapping properties (4.17) and the product formula [9]

$$B_i^n(t)B_j^m(t) = \frac{\binom{n}{i}\binom{m}{j}}{\binom{n+m}{i+j}} B_{i+j}^{n+m}(t), \tag{4.21}$$

it follows that δ maps any planar rational Bézier curve of degree n to a rational Bézier curve of degree $2n$ on the unit sphere $\mathbb{S}^2$.

4.4. **Circular boundary curves.** We will now parametrize a circular arc $\mathcal{C} \subset \mathbb{S}^2$ by the inverse δ of the generalized stereographic projection. There are already plenty of methods [17, 18, 31] for representing a circular arc as a rational Bézier curve but we explicitly need that it is an image of δ to realize global continuity according to (2.10).

Let $\mathbf{c}_0, \mathbf{c}_3 \in \mathcal{C}$ be the endpoints of the arc $\mathcal{C}$ and consider the two interior points $\mathbf{c}_1, \mathbf{c}_2 \in \mathcal{C}$ such that $\|\mathbf{c}_0 - \mathbf{c}_1\| = \|\mathbf{c}_1 - \mathbf{c}_2\| = \|\mathbf{c}_2 - \mathbf{c}_3\|$ as illustrated in Fig. 6(a). Let further be $\mathbf{b}_0, \mathbf{b}_2 \in \mathbb{E}^3$ the preimages of the endpoints computed by (4.19), i.e., $\mathbf{c}_0 = \delta(\mathbf{b}_0)$ and $\mathbf{c}_3 = \delta(\mathbf{b}_2)$. We want to determine a rational Bézier curve $\mathbf{X}(t)$, satisfying $\mathbf{X}(0) = \mathbf{b}_0$ and $\mathbf{X}(1) = \mathbf{b}_2$, which is mapped by δ onto the circular arc $\mathcal{C}$. This amounts to (see [9]) finding the internal node $\mathbf{b}_1 \in \mathbb{E}^3$ such that the following homogeneous quadratic Bézier curve

$$\mathbf{X}(t) = \mathbf{b}_0 B_0^2(t) + \mathbf{b}_1 B_1^2(t) + \mathbf{b}_2 B_2^2(t) \quad \text{with} \quad \mathbf{b}_i = [w_i : x_i : y_i : z_i] \tag{4.22}$$

satisfies $\mathcal{C} = \delta\big(\mathbf{X}(t)\big)$.

We claim $\mathbf{c}_1 = \delta\big(\mathbf{X}(1/3)\big)$ and $\mathbf{c}_2 = \delta\big(\mathbf{X}(2/3)\big)$. To solve this problem we compute, in accordance with (4.20), $\mathbf{q}_i \in \mathbb{E}^3$ such that $\delta(\mathbf{q}_i) = \mathbf{c}_i$, $i = 1, 2$. Recall that $\delta^{-1}(\mathbf{c}_i) = \{\lambda\mathbf{q}_i + \mu\mathbf{q}_i^\perp : \lambda, \mu \in \mathbb{R}\}$ (cf. (4.19)), and hence, for $t_1 = 1/3$, $t_2 = 2/3$, it follows that

$$\langle \overline{\mathbf{q}}_i, \mathbf{X}(t_i)\rangle = 0 \quad \text{and} \quad \langle \overline{\mathbf{q}}_i^\perp, \mathbf{X}(t_i)\rangle = 0, \qquad i = 1, 2.$$

By defining for $\mathbf{q} \in \mathbb{E}^3$ and $t \in \mathbb{R}$

$$K(\mathbf{q}, t) := -\frac{1}{B_1^2(t)} \left[\langle \mathbf{q}, \mathbf{b}_0\rangle B_0^2(t) + \langle \mathbf{q}, \mathbf{b}_2\rangle B_2^2(t)\right], \tag{4.23}$$

we thus arrive at

$$\langle \overline{\mathbf{q}}_i, \mathbf{b}_1\rangle = K(\overline{\mathbf{q}}_i, t_i), \quad \langle \overline{\mathbf{q}}_i^\perp, \mathbf{b}_1\rangle = K(\overline{\mathbf{q}}_i^\perp, t_i), \qquad i = 1, 2. \tag{4.24}$$

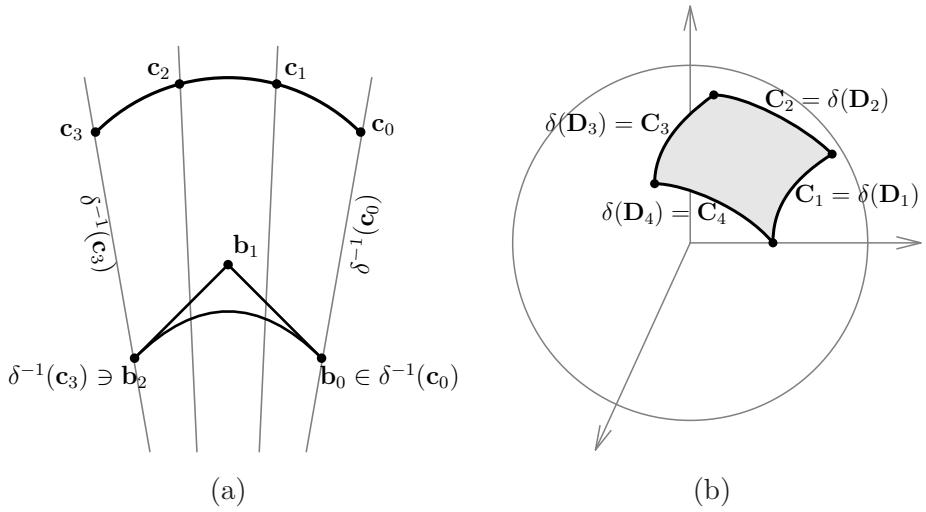

FIGURE 4.6. (a) A conic maps to the circle by the generalized stereographic projection δ (b) Spherical patch delineated by four circular arcs.

The relations (4.23), (4.24) lead to a linear (4×4)-system for the unknown coordinates w_1, x_1, y_1, z_1 of $\mathbf{b}_1$.

Since $\mathbf{X}(t)$ from (4.22) is a Bézier curve of degree two in homogeneous coordinates, its image by δ is a homogeneous Bézier curve of degree four. Thus, in Cartesian coordinates, the quartic rational Bézier $\delta\big(\mathbf{X}(t)\big)$ is the sought parametrization of the arc $\mathcal{C}$.

4.5. **Spherical patches.** Let us consider four circular arcs $\mathcal{C}_k \subset \mathbb{S}^2$, represented as rational Bézier curves $\mathbf{C}_k$, i.e. $\mathcal{C}_k = \mathbf{C}_k([0,1])$, which enclose the four-sided spherical surface $\mathcal{T}$. By using degree elevations, we can suppose that the $\mathbf{C}_k(t)$ have same degrees, i.e.,

$$\mathbf{C}_k(t) = \sum_{i=0}^{2n} \mathbf{c}_i^k B_i^{2n}(t) \quad \text{with} \quad \mathbf{c}_i^k = [w_i^k : x_i^k : y_i^k : z_i^k], \qquad k = 1,2,3,4.$$

In accordance with the previous subsection, we may assume that they are the images of four Bézier curves $\mathbf{D}_k(t)$ of degree n

$$\mathbf{C}_k(t) = \delta\big(\mathbf{D}_k(t)\big) \quad \text{with} \quad \mathbf{D}_k(t) = \sum_{i=0}^{n} \mathbf{d}_i^k B_i^n(t), \qquad k = 1,2,3,4,$$

such that there is coincidence at the corners

$$\mathbf{d}_0^1 = \mathbf{d}_0^4, \quad \mathbf{d}_n^1 = \mathbf{d}_0^2, \quad \mathbf{d}_n^2 = \mathbf{d}_n^3, \quad \mathbf{d}_0^3 = \mathbf{d}_n^4,$$

see also Fig. 6(b).

We are searching for a *spherical transfinite interpolant* $\mathbf{X}(u,v)$, residing on $\mathbb{S}^2$, which coincides at the boundaries with the curves $\mathbf{C}_k(t)$. That is, we want to find a spherical patch $\mathbf{X}:\square\to\mathcal{T}$, satisfying

$$\begin{aligned}\mathbf{X}(u,0)&=\mathbf{C}_1(u), \qquad \mathbf{X}(u,1)=\mathbf{C}_3(u), \qquad \forall u\in[0,1],\\ \mathbf{X}(0,v)&=\mathbf{C}_4(v), \qquad \mathbf{X}(1,v)=\mathbf{C}_2(v), \qquad \forall v\in[0,1],\end{aligned} \tag{4.25}$$

and $\mathbf{X}(\square)=\mathcal{T}$. The desired patch $\mathbf{X}(u,v)$ will be represented as a rational Bézier surface that has the following form in homogeneous coordinates

$$\mathbf{X}(u,v)=\sum_{i,j=0}^{2n}\mathbf{b}_{ij}B_i^{2n}(u)B_j^{2n}(v) \quad \text{with} \quad \mathbf{b}_{ij}=[w_{ij}:x_{ij}:y_{ij}:z_{ij}].$$

Due to the properties of δ in (4.19) and (4.21), that problem amounts to searching for some rational Bézier surface $\mathbf{Y}$ of degree n,

$$\mathbf{Y}(u,v)=\sum_{i,j=0}^{n}\mathbf{a}_{ij}B_i^n(u)B_j^n(v),$$

satisfying $\mathbf{Y}(u,v)=\delta\big(\mathbf{X}(u,v)\big)$. Thus, the problem is reduced to the determination of the homogeneous control points $\mathbf{a}_{ij}$ of $\mathbf{Y}(u,v)$. On account of the boundary conditions (4.25), the boundary control points should be chosen as

$$\mathbf{a}_{i0}:=\mathbf{d}_i^1, \quad \mathbf{a}_{in}:=\mathbf{d}_i^3, \quad \mathbf{a}_{0j}:=\mathbf{d}_j^4, \quad \mathbf{a}_{nj}:=\mathbf{d}_j^2, \quad \forall i,j=0,\dots,n. \tag{4.26}$$

It remains to determine the internal control points $\mathbf{a}_{ij}$ which we specify by the following interpolation problem

$$\mathbf{X}(u_k,v_k)=\delta\big(\mathbf{Y}(u_k,v_k)\big)=\mathbf{p}_k, \quad k=1,\dots,m:=2(n-1)^2,$$

for given corresponding internal pairs $\mathbf{p}_k\in\mathcal{T}\subset\mathbb{S}^2$ and $(u_k,v_k)\in(0,1)^2$.

Let $\mathbf{q}_k$ be the preimage of $\mathbf{p}_k$ computed by (4.20), i.e., $\mathbf{p}_k=\delta(\mathbf{q}_k)$. We shall determine the control points $\mathbf{a}_{ij}$ such that the interpolation problem $\mathbf{Y}(u_k,v_k)=\mathbf{q}_k$ is satisfied for all $k=1,\dots,m$. Similar to the previous subsection, on account of (4.18) and (4.19), we arrive at

$$\langle\overline{\mathbf{q}}_k,\mathbf{Y}(u_k,v_k)\rangle=0, \quad \langle\overline{\mathbf{q}}_k^{\perp},\mathbf{Y}(u_k,v_k)\rangle=0, \quad k=1,\dots,m. \tag{4.27}$$

By denoting the set of indices (i,j) of internal and boundary control points of $\mathbf{Y}(u,v)$ by $\mathcal{J}$ and $\mathcal{B}$ respectively, (4.27) can be rewritten by

$$\begin{aligned}\sum_{(i,j)\in\mathcal{J}}\langle\overline{\mathbf{q}}_k,\mathbf{a}_{ij}\rangle B_i^n(u_k)B_j^n(v_k)&=-\sum_{(i,j)\in\mathcal{B}}\langle\overline{\mathbf{q}}_k,\mathbf{a}_{ij}\rangle B_i^n(u_k)B_j^n(v_k),\\ \sum_{(i,j)\in\mathcal{J}}\langle\overline{\mathbf{q}}_k^{\perp},\mathbf{a}_{ij}\rangle B_i^n(u_k)B_j^n(v_k)&=-\sum_{(i,j)\in\mathcal{B}}\langle\overline{\mathbf{q}}_k^{\perp},\mathbf{a}_{ij}\rangle B_i^n(u_k)B_j^n(v_k),\\ &\qquad\qquad k=1,\dots,m.\end{aligned} \tag{4.28}$$

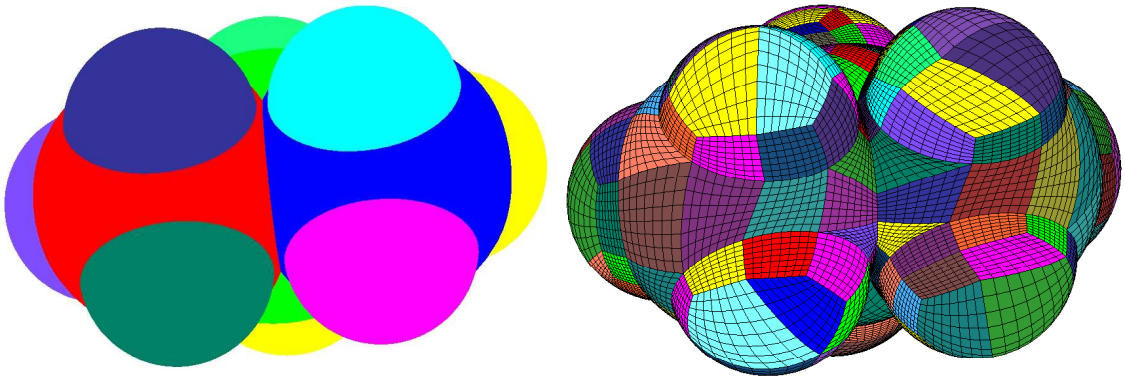

FIGURE 5.7. Propane (11 atoms) is decomposed into 231 four-sided patches.

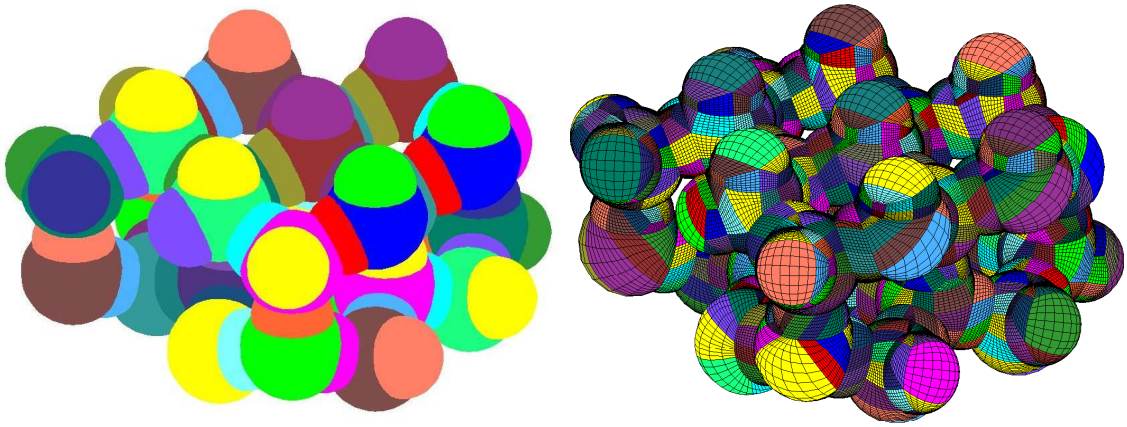

FIGURE 5.8. An ice molecule with 84 atoms is decomposed into 1284 four-sided patches.

Since the control points $\mathbf{a}_{ij}$ for $(i,j) \in \mathcal{B}$ are specified by (4.26), the right hand side of (4.28) is known. Therefore, this leads to some linear system of equations for the unknown coefficients $\mathbf{a}_{ij}$ with $(i,j) \in \mathcal{J}$.

5. Numerical results

5.1. **Molecular surfaces.** We have implemented routines in C/C++ and OpenGL in order to split molecular surfaces into patches. Although the conversion of the constructive solid geometry (CSG) representation into a B-rep structure (3.15) according to Section (3) sounds not too hard, its implementation constitutes a large part of the program. Moreover, this step consumes about 70% of the computing time.

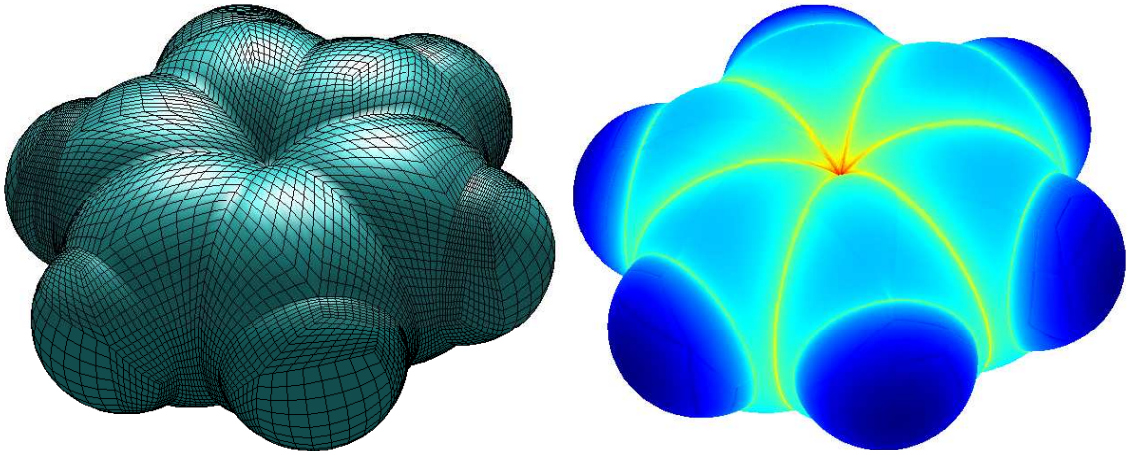

FIGURE 5.9. Parametric representation of benzene and computed apparent surface charge

Two examples of decomposition into four-sided surfaces can be seen in Fig. 5.7 and Fig. 5.8. They correspond to the molecules of propane and ice which have respectively 11 and 84 atoms. The final decompositions have respectively 231 and 1284 four-sided patches. The pentane molecule in Fig. 1(a), consisting of 17 atoms, has been decomposed into 388 four-sided patches shown in Fig. 1(b). We mention that the computing time for decomposing the molecular surface into four-sided patches lies always in the range 1/2–1 minute.

5.2. **BEM solver.** To demonstrate and test our BEM implementation we choose a benzene molecule, for which the present algorithm produces a parametrization with $M = 160$ patches. The mesh on level three is depicted in Fig. 5.9. We discretize the integral operators $\mathcal{A}$ and $\mathcal{V}$ as described in Subsection 2.3 by piecewise constant wavelets with three vanishing moments. We place point charges at the nuclei positions and compute the apparent surface charge according to both integral equations (2.7) and (2.8). The dielectric constant has been chosen as $\varepsilon = 100$.

We computed the apparent surface charge on discretization levels 1–5. The solution on level 5 is visualized in the right plot of Fig. 5.9. The compression rates and computing times are reported in the three last columns of Tab. 5.1. On level $J = 5$, i.e., $N_J = 163840$ unknowns, we need in the mean about 500 matrix entries per degree of freedom after the a-priori compression. The a-posteriori compression reduces this number to 170 matrix entries per degree of freedom.

J	N_J	E_1	E_2	cpu-time (in sec.)	a-priori compression (nnz in %)	a-posteriori compression (nnz in %)
1	640	0.0873715	0.689489	0	22	17
2	2560	0.0655432	0.241627	6	8.5	6.8
3	10240	0.0405458	0.0519634	37	3.4	2.0
4	40960	0.0205933	0.000654688	356	1.1	0.44
5	163840	0.00284775	0.0000436096	2330	0.31	0.10

TABLE 5.1. Numerical results with respect to the benzene.

To measure the accuracy of the unknown solution we compute the *total charge* $T(\rho)$ according to (cf. (2.6))

$$T(\rho) = \int_\Omega \rho d\mathbf{x} = \int_\Gamma \frac{\partial u_i}{\partial \mathbf{n}} do = \frac{1-\varepsilon}{\varepsilon} \int_\Gamma \sigma do.$$

Let $\sigma_J^{1)}$ and $\sigma_J^{2)}$ denote the apparent surface charges computed from the boundary integral equations (2.7) and (2.8), respectively. In columns 3 and 4 of Tab. 5.1 we computed the approximation errors $E_i = \left|T(\rho) - T_J^{(i)}(\rho)\right|$, $i = 1, 2$, with respect to the total charge. One figures out of Tab. 5.1 that the second integral equation induces much better results. This issues from the fact that the right hand side N_ρ is much smoother than the right hand side of the first integral equation which contains the data of $\partial N_\rho / \partial \mathbf{n}$.

REFERENCES

[1] G. Beylkin, R. Coifman, and V. Rokhlin. The fast wavelet transform and numerical algorithms. *Comm. Pure and Appl. Math.* **44** (1991) 141–183.

[2] G. Brunnett. Geometric design with trimmed surfaces. *Computing Supplementum* **10** (1995) 101–115.

[3] E. Cancés and B. Mennucci. New applications of integral equations methods for solvation continuum models: ionic solutions and liquid crystals. *J. Math. Chemistry* **23** (1998) 309–326.

[4] M. Connolly. Molecular surface guide, 2006, http://connolly.best.vwh.net.

[5] W. Dahmen, H. Harbrecht, and R. Schneider. Compression techniques for boundary integral equations — optimal complexity estimates. *SIAM J. Numer. Anal.* **43** (2006) 2251–2271.

[6] W. Dahmen and A. Kunoth. Multilevel preconditioning. *Numer. Math.* **63** (1992) 315–344.

[7] W. Dahmen, A. Kunoth, and K. Urban. Biorthogonal spline wavelets on the interval: stability and moment conditions. *Appl. Comput. Harmon. Anal.* **6** (1999) 132–196.

[8] R. Dietz, J. Hoschek, and B. Jüttler. Rational patches on quadric surfaces, *Comput.-Aided Des.* **27** (1995) 27–40.

[9] G. Farin. *Curves and Surfaces for CAGD: A Practical Guide*. Academic Press, 1999.

[10] L. Frediani, R. Cammi, S. Corni, and J. Tomasi. *A polarizable continuum model for molecules at diffuse interfaces. J. Chem. Phys.* **120** (2004) 3893–3907.

[11] L. Greengard and V. Rokhlin. A fast algorithm for particle simulation. *J. Comput. Phys.* **73** (1987) 325–348.

[12] W. Hackbusch and B.N. Khoromskij. A sparse $\mathcal{H}$-matrix arithmetic. II: Application to multi-dimensional problems. *Computing* **64** (2000) 21–47.

[13] W. Hackbusch and Z.P. Nowak. On the fast matrix multiplication in the boundary element method by panel clustering. *Numer. Math.* **54** (1989) 463–491.

[14] H. Harbrecht and M. Randrianarivony. From Computer Aided Design to wavelet BEM. *Bericht 07-18*, Berichtsreihe des Mathematischen Seminars, Christian-Albrechts-University of Kiel, Germany, 2007. (to appear in Comput. Vis. Sci.).

[15] H. Harbrecht and R. Schneider. Biorthogonal wavelet bases for the boundary element method. *Math. Nachr.* **269–270** (2004) 167–188.

[16] H. Harbrecht and R. Schneider. Wavelet Galerkin Schemes for Boundary Integral Equations – Implementation and Quadrature. *SIAM J. Sci. Comput.* **27** (2002) 1347–1370.

[17] J. Hoschek and D. Lasser. *Fundamentals of computer aided geometric design*. A.K. Peters, Wellesley, 1993.

[18] Q. Hu and G. Wang. Necessary and sufficient conditions for rational quartic representation of conic sections. *J. Comput. Appl. Math.* **203** (2007) 190–208.

[19] B. Korte and J. Vygen. *Combinatorial Optimization: Theory and Algorithms*. 3rd ed., Springer-Verlag, Berlin Heidelberg New York, 2006.

[20] P. Laug and H. Borouchaki. Molecular surface modeling and meshing. *Engineering with Computers* **18** (2002) 199–210.

[21] S. Miertuš, E. Scrocco and J. Tomasi. Electrostatic Interaction of a Solute with a Continuum. A Direct Utilization of Ab Initio Molecular Potentials for the Prevision of Solvent Effects. *Chem. Phys.* **55** (1981) 117–129.

[22] C.S. Pomelli. Cavity surfaces and their discretization. in: *Continuum Solvation Models in Chemical Physics: From Theory to Applications*. Benedetta Mennucci (Editor), Roberto Cammi (Co-Editor), pp. 49–63, Wiley, 2007.

[23] L. Piegl and W. Tiller. *The NURBS book*. Springer, Berlin, 1995.

[24] M. Randrianarivony. *Geometric processing of CAD data and meshes as input of integral equation solvers*. PhD thesis, Technische Universität Chemnitz, 2006.

[25] M. Randrianarivony. *Quadrilateral decomposition by two-ear property resulting in CAD segmentation*. Proc. Fifth International Conference on Computational Geometry, pp. 179–185, 2008.

[26] M. Randrianarivony and G. Brunnett. Molecular Surface Decomposition using Graphical Modeling. in *Bildverarbeitung für die Medizin: Algorithmen — Systeme — Anwendungen*, Proceedings des Workshops vom 6. bis 8. April 2008 in Berlin, Springer-Verlag, Berlin Heidelberg, pp. 197–201, 2008.

[27] M. Sanner, A. Olsen, and J. Spehner. Reduced surface: an efficient way to compute molecular surfaces. *Biopolymers* **38** (1996) 305–320.

[28] R. Schneider. *Multiskalen- und Wavelet-Matrixkompression: Analysisbasierte Methoden zur Lösung großer vollbesetzter Gleichungssysteme.* Teubner, Stuttgart, 1998.

[29] O. Steinbach. *Numerical Approximation Methods for Elliptic Boundary Value Problems. Finite and Boundary Elements.* Springer, New York, 2008.

[30] J. Tomasi, B. Mennucci, and R. Cammi. Quantum Mechanical Continuum Solvation Models. *Chem. Rev.* **105** (2005) 2999–3094.

[31] G.-J. Wang and G.-Z. Wang. The rational cubic Bézier representation of conics. *Computer Aided Geometric Design* **9** (1992) 447–455.

[32] D. Whitley. Van der Waals graphs and molecular shape. *J. Math. Chem.* **23** (3–4) (1998) 377–397.

Helmut Harbrecht and Maharavo Randrianarivony, Institut für Numerische Simulation, Universität Bonn, Wegelerstr. 6, 53115 Bonn, Germany.

E-mail address: {harbrecht,randrian}@ins.uni-bonn.de